Downloaded from https://academic.oup.com/mnras/article/502/2/2158/6070633 by National Astronomical Observatory user on 12 July 2021

MNRAS **502**, 2158–2171 (2021) Advance Access publication 2021 January 8

Global optimization-based reference star differential imaging for high-contrast exoplanet imaging survey

Deqing Ren^{1★} and Yili Chen^{2,3,4★}

- ¹California State University Northridge, Northridge, CA 91330, USA
- ²National Astronomical Observatories/Nanjing Institute of Astronomical Optics and Technology, Chinese Academy of Sciences, Nanjing 210042, China
- ³CAS Key Laboratory of Astronomical Optics and Technology, Nanjing Institute of Astronomical Optics and Technology, Nanjing 210042, China

Accepted 2020 December 30. Received 2020 December 26; in original form 2020 September 17

ABSTRACT

We propose a data reduction approach called global optimization-based reference star differential imaging (G-RDI), which can be used for exoplanet imaging survey, where large numbers of target stars from the same young stellar association are imaged and where no field rotation is needed. One of the unique features of our G-RDI is that we select reference stars from other scientific target stars in the same stellar association to optimize for high-contrast imaging with a target star, which maximizes the observational efficiency and also delivers good performance to remove the speckle noise so that high contrast is achievable even at a small inner working angle (IWA) to the host star of being imaged. We proposed the G-RDI that is optimized for high-contrast exoplanet imaging at a small IWA and to provide a contrast that is significantly better than the current reference star differential imaging (RDI) method. In addition, we also propose the use of multiple reference stars and found that our G-RDI can further deliver better performance in that case. The result was compared with other exoplanet data reduction techniques, including the traditional RDI, and it indicated that our G-RDI with two reference stars can significantly improve the contrast performance at a small IWA with a high observational efficiency – two critical features that current data reduction techniques cannot offer. This approach could be used with both equatorial and alt-azimuth mount telescopes, and provides a new option for future exoplanet imaging surveys with high observational efficiency at a small IWA.

Key words: instrumentation: adaptive optics – methods: data analysis – techniques: image processing.

1 INTRODUCTION

Exoplanet imaging is one of the research priorities in astrophysical science, and many flagship telescopes are being used for dedicated exoplanet imaging survey programs, with the goal to find and characterize new exoplanets. These include the Gemini Planet Imager (GPI) with the 8-m Gemini telescope (Macintosh et al. 2008, 2014, 2015), the Spectro-Polarimetric High-contrast Exoplanet REsearch (SPHERE) with the 8-m Very Large Telescope (Beuzit et al. 2008), the Strategic Exploration of Exoplanets and Disks with Subaru (SEEDS) with the 8-m Subaru telescope (Uyama et al. 2017), and so on; see the detailed surveys recently provided by Bowler (2016). Today, a few dozes of young and giant exoplanets, such as the HR 8799 (Marois et al. 2008a, 2010), HD 95086 b (Meshkat et al. 2013; De Rosa et al. 2016), Beta Pictoris b (Lagrange et al. 2010; Bonnefoy et al. 2011), and 51 Eridani b (Macintosh et al. 2015), were discovered by imaging in the near-infrared (NIR), in which dedicated data reduction methods were adopted. Exoplanet imaging suffers from the so-called quasi-static and dynamical speckles, which are the dominant noises for the imaging of faint exoplanets. The dynamic speckle noise can be effectively suppressed by averaging a large number of short-exposure images. However, when the exposure

time increases (or equivalently to averaging a large number of short-exposure images), the intensity of quasi-static speckle will also increase accordingly, and thus it could not be removed, by simply increasing the exposure time. The quasi-static speckle noise could originate from the optical aberrations of the telescope and associated instrumentation, and it must be effectively suppressed before high-contrast exoplanet imaging is possible (Bloemhof 2004; Soummer & Aime 2004; Fitzgerald & Graham 2006; Hinkley et al. 2007; Soummer et al. 2007; Marois et al. 2008b; Mawet et al. 2014; Ruffio et al. 2017).

For ground-based exoplanet imaging, observations have shown that for integrations longer than a few minutes, the point spread function (PSF) noise converges to a quasi-static noise pattern, thus preventing a gain with increasing integration time (Marois et al. 2005; Masciadri et al. 2005). To effectively remove this quasi-static speckle noise for imaging of faint exoplanets nearby bright stars, angular differential imaging (ADI; Marois et al. 2006) was proposed. ADI is based on field rotation, i.e. the astrophysical image is rotated along with the field rotation, which provides a means to average the quasi-static noise. Based on the same idea, Locally Optimized Combination of Images (LOCI; Lafreniere et al. 2007) further divides the entire PSF image into small subsections and minimizes the residual noise in each area (Lafreniere et al. 2007). Many methods based on the ADI were developed in past years, such as the damped LOCI (Pueyo et al. 2012), the Adaptive LOCI (ALOCI; Currie et al. 2013), the

⁴University of Chinese Academy of Sciences, Beijing 100049, China

^{*} E-mail: ren.deqing@csun.edu (DR); ylchen@niaot.ac.cn (YC)

Template LOCI (TLOCI; Marois et al. 2014), and the Matched LOCI (MLOCI; Wahhaj et al. 2015). There are also some methods that are based on the principal component analysis (PCA) to suppress the speckle noise. The typical methods are the Karhunen–Lóeve Image Processing (KLIP; Soummer, Pueyo & Larkin 2012) and the PYNPOINT (Amara & Quanz 2012; Amara, Quanz & Akeret 2015). It was reported that the PYNPOINT can achieve better performance at a smaller inner working angle (IWA), while avoiding oversubtraction of the companion flux (Amara & Quanz 2012).

Unfortunately, all the above reduction methods used for today's exoplanet imaging can only work with an alt-azimuth mount telescope, since they are designed to reduce images with a field rotation and thus are not suitable for exoplanet imaging with an equatorial mount telescope that has no such a field rotation. For an equatorial telescope, reference star differential imaging (RDI; Lafrenière et al. 2009; Soummer et al. 2011; Gerard & Marois 2016) can be used to build a model of the stellar PSF, used to subtract the speckle noise of the target star. RDI was used with *Hubble Space Telescope* imaging observations of debris discs (Golimowski et al. 2006; Schneider et al. 2009, 2014; Choquet et al. 2016). Because the subtraction is done via the modelled stellar PSF, it can be used with both of a ground-based equatorial mount and an alt-azimuth mount telescope.

Image Rotation and Subtraction (IRS) and Optimized Image Rotation and Subtraction (OIRS) developed by Ren et al. (2012) and Dou et al. (2015), respectively, provide another possibility to achieve high-contrast imaging at a small IWA, with an equatorial mount telescope. IRS is a method that a target image is subtracted with its own 180° rotational image to attenuate the potential quasistatic noise, because all even orders of the speckle noise can be totally subtracted. OIRS uses small subsections of the PSF image to further minimize the residual noise in each subsection similar to that of the LOCI. In principle, both the IRS and OIRS could be used with an equatorial telescope. However, the speckle noise corresponding to the odd terms of the wavefront error may still be a dominant noise, which may eventually limit the performance for the high-contrast exoplanet imaging.

While one of the key conclusions from the previous exoplanet imaging surveys has been that massive gas giant planets are rare in orbits with separations larger than a few tens of astronomical units, the innermost regions around the stars are still largely unexplored as we lack the required contrast (Amara & Quanz 2012). This is especially true for faint-star exoplanet imaging, since the faint star limits the available photons for the adaptive optics (AO) wavefront sensing and thus the associated AO system can only provide a limited wavefront correction. Deeper contrasts and smaller IWAs will increase the pace of discovery to ultimately map the demographics, composition, evolution, and origin of planets spanning a broad range of masses and ages, which will be a future direction for exoplanet imaging (Bowler 2016). While the ADI-associated techniques are powerful for high-contrast exoplanet imaging, they have some innate limitations (Ruane et al. 2019), including observational timing constraints, limited sky coverage, inefficient surveys of starforming regions, limited effective IWA, which make it impossible for highly efficient observations with the ADI-associated data reduction techniques.

Using the RDI technique, Lagrange et al. (2009) successfully detected the exoplanet Beta Pictoris b that has a normalized contrast of $\sim 10^{-3}$ at the L' band with an IWA of $3.8\lambda/D$ to its host star. Since no field rotation is needed, the RDI has the potential to be used for the detection of the exoplanet at a small IWA. However, the use of a reference star may induce a systematic error, which would induce a quasi-static speckle noise that eventually limits its

performance. Since the detection of the Beta Pictoris b, almost all exoplanets, found by direct imaging, are detected by using the ADIbased techniques, because the ADI can effectively suppress the quasistatic speckle noise (Marois et al. 2006), and thus deliver a better performance. In the recent years, the RDI technique is being further used for ground-based exoplanet imaging for vortex coronagraph observations that were initially tested with the Hale Telescope at the Palomar Observatory (Serabyn, Mawet & Burruss 2010) and currently were conducted with the Keck II at the W. M. Keck Observatory (Mawet et al. 2010, 2011; Xuan et al. 2018; Ruane et al. 2019), in which the recent tests at the L' band (3.776 μ m central wavelength) indicated that the coronagraph and RDI combination delivers a better contrast at an IWA smaller than the $3.2\lambda/D$, while at a larger angular distance the ADI delivers a better performance. At the 3.2 λ/D IWA, the system delivers a median contrast of $\sim 10^{-2.5}$, and a best contrast $\sim 10^{-3.5}$ (Xuan et al. 2018), while combined with the frame selection method the contrast can be improved by a factor of 3 (Ruane et al. 2019).

In past decades, a number of exoplanet imaging surveys have been conducted. However, only a few dozens of exoplanets were detected (Bowler 2016). While this proves that exoplanet imaging is a challenging task, it also clearly indicates that further improving the observation efficiency that may lead to large number of discoveries is urgent. Given the fact of the low occurrence for exoplanet imaging, on the order of about 1 per cent (Bowler & Nielsen 2018), high observational efficiency for exoplanet imaging is critical for the discoveries of new exoplanets. In this paper, we propose a reference-star-based optimization technique, which can well address the potential systematic error of the current RDI techniques, and provide a significantly high observation efficiency and high contrast performance at a small IWA that the current ADI-associated techniques cannot offer. Our reference star optimization technique is simple to implement and no coronagraph is needed. It can deliver a good contrast, even at the short wavelength of the K band with a moderate AO performance, which implies that it has the potential to be used for imaging of exoplanets hosted by faint stars that are largely untouched. The rest of this paper is arranged as follows. In Section 2, we present our reference-star-based optimization algorithm. In Section 3, the target star HIP 72389 is used as an example to demonstrate our referencestar-based optimization approach with different selected optimized regions and with different numbers of reference stars. In Section 4, we compare our reference-star-based optimization with other exoplanet imaging reduction methods and the photon noise limited case. In Section 5, as an initial application for exoplanet imaging with the 200-inch Hale Telescope at the Palomar Observatory, we list our one-night observational results of low-mass companion candidate imaging that are reduced with our reference-star-based optimization. In Section 6, we measure the flux of artificial planets in small IWA and compare them with the true flux of artificial planets. We analyse our global optimization-based reference star differential imaging (G-RDI) performance limitation in Section 7. Finally, we achieve our conclusion in Section 8.

2 ALGORITHM FOR GLOBAL OPTIMIZATION-BASED REFERENCE STAR DIFFERENTIAL IMAGING

For equatorial telescopes, the exiting high-contrast image data reduction methods that are based on field rotation, such as the ADI-associated algorithms (Marois et al. 2006; Lafreniere et al. 2007), cannot be directly applied to imaging data taken from these telescopes, since there is no image rotation. To construct a reference

PSF for effective speckle noise subtraction from the target images, a new methodology is needed.

Since our reference-star-based optimization is dedicated to the exoplanet imaging survey where a large number of target stars will be imaged from the same stellar association, we select a scientific target star from the same association as a reference star. We adopt a mathematical optimization approach similar to that used in the LOCI in the ADI-associated data reductions (Lafreniere et al. 2007), since it will allow every target image to be optimized with all the reference star images, minimizing the residual noise. In addition, this algorithm is easy to implement for our reference-star-based optimization. Since no image rotation is required, our reference-star-based optimization methodology should have the potential to deliver a better contrast at a small IWA, which is a significant advantage for future groundbased exoplanet imaging programs. For exoplanet imaging of a young stellar association, the scientific targets, in general, would have similar spectra, which will allow effective speckle noise subtraction. In addition, they are located in close positions in the sky, thus sharing similar celestial coordinates. These features indicate that we can effectively use one of the target stars as a reference star to subtract with other target stars. For simplicity, we assume that both target and reference stars have the same image number, and N is the total image number for each group of the target and reference images, respectively. For all the reference images, a reference PSF can be constructed with the following equation:

$$I^{R} = \sum_{k} c^{k} I^{k}, \tag{1}$$

where I^R is the reconstructed PSF from all images of the reference star. k=1,2,...,N is the index number of k image. c^k is the associated coefficients that should be found by optimization for best subtraction of the speckle noise for the exoplanet imaging in such a way that each target image is effectively subtracted with the reconstructed reference PSF. For such a subtraction, the reference PSF is the result of the optimization over a pre-defined optimization region that may have dominant speckle noise. At pixel i of the image, we have the target image I_i^T and the reconstructed reference PSF I_i^R . The squared residual of such subtractions applied on all image pixels in the optimization region is

$$\sigma^{2} = \sum_{i} (I_{i}^{T} - I_{i}^{R})^{2} = \sum_{i} \left(I_{i}^{T} - \sum_{k} c^{k} I_{i}^{k} \right)^{2}.$$
 (2)

Note that for each target image I^T , a corresponding reference I^R is reconstructed. That is, the reference PSF is different for each target image, which ensures an optimization subtraction for each of the target images. To minimize the σ^2 for the speckle noise subtraction, all partial derivatives of σ^2 respect to the coefficients c^k need to be zero. Thus, we have the following equation:

$$\frac{\partial \sigma^2}{\partial c^j} = \sum_i -2I_i^j \left(I_i^{\mathrm{T}} - \sum_k c^k I_i^k \right) = 0. \tag{3}$$

Rearrange the above equation, we have

$$\sum_{k} c^{k} \left(\sum_{i} I_{i}^{j} I_{i}^{k} \right) = \sum_{k} I_{i}^{j} I_{i}^{\mathrm{T}}. \tag{4}$$

These linear equations can be expressed in a matrix form as Ax = b, with

$$A_{jk} = \sum_{i} I_i^j I_i^k, \quad x_k = c^k, \quad b_j = \sum_{i} I_i^j I_i^{\mathrm{T}}.$$
 (5)

The goal of the above optimization is to find the coefficient vector x for each target image. Since the equations are redundant, we can use singular value decomposition (SVD) to find the pseudo-inverse of A and thus solve the coefficient vector x. In this case, A can be decomposed as $U\Sigma V^T$, where Σ , U, and V are the diagonal matrix, left and right singular vectors, respectively. The pseudo-inverse of A is $A^+ = V\Sigma^+ U^T$. Here, Σ^+ is the pseudo-inverse of Σ , which is formed by replacing every non-zero diagonal entry with its reciprocal and transposing the resulting matrix. Therefore, we have

$$c = A^+ b. (6)$$

For a group of *N* target images, each target image can be subtracted with its corresponding reconstructed reference PSF that can be found with the above equations. The above algorithm is used by the LOCI for the ADI, where field rotation is required. This approach, however, has not been used for the RDI with a discovery of exoplanet. For the RDI, no field rotation is available. Therefore, special measures must be taken to deal with this issue, as we will discuss in later sections.

In fact, the *N* subtracted target images acquired with the above equations can be further optimized to deliver a better contrast. Here, we propose an algorithm, in which every subtracted target image is multiplied with a scale factor and these scaled images are summed together to optimize for the best subtraction of the speckle noise, without removing the exoplanet signal. We call it G-RDI. If we summed these scaled images and directly optimize them, without a restraint, all signals, including that of the exoplanet and speckle, will be subtracted to zero, since an immediate resolution exists, in which all the scale factors for each subtract image are equal to zero. Therefore, we must optimize these scale factors, under a specific constraint condition. For our G-RDI, we can define a Lagrangian function to solve the minimum value problem with a constraint to limit the scale factors:

$$L = \sum_{i} \sum_{k} (s^{k} I_{i}^{k})^{2} + \lambda \psi(s^{1}, s^{2}, \dots, s^{k}), \tag{7}$$

with
$$\psi(s^1, s^2, \dots, s^k) = \sum_{k} (s^k) - N,$$
 (8)

where i is the pixel index number in each image. k is the target image index number, which is in the range between 1 and N. s^k is the scale factor for each image. s^1 , s^2 , ..., s^k and λ are the parameter that need to be optimized. In equation (7), the first part on the right-hand side is the function that will be optimized for a minimum value, while the second part is the constraint condition that we defined. The function to be optimized is defined as the sum of the square of the pixel value in an optimized region with all the scaled images. Here, we define the sum of all scale factors must be constrained to be equal to N. That is, the exoplanet signal must be kept as a constant that is equal to the original value before the optimization and thus this constraint will ensure no exoplanet signal will be subtracted.

To minimize the Lagrangian function, all partial derivatives of L respect to the coefficients s^k and λ need to be zero. Thus, we get the following equations:

$$\frac{\partial L}{\partial s^j} = \sum_i \left(2I_i^j \sum_k (s^k I_i^k) \right) + \lambda = 0, \tag{9}$$

$$\frac{\partial L}{\partial \lambda} = \sum_{k} (s^k) - N = 0. \tag{10}$$

Rearrange the above equations, we have

$$2\sum_{i}\sum_{k}(s^{k}I_{i}^{k}I_{i}^{j}) + \lambda = 0, \tag{11}$$

$$\sum_{k} (s^k) = N, \tag{12}$$

which can be expressed in the matrix form as By = d, with

$$B = \begin{bmatrix} 2\sum_{i}(I_{i}^{1}I_{i}^{1}) & \cdots & 2\sum_{i}(I_{i}^{1}I_{i}^{N}) & 1\\ \cdots & \cdots & \cdots & 1\\ 2\sum_{i}(I_{i}^{N}I_{i}^{1}) & \cdots & 2\sum_{i}(I_{i}^{N}I_{i}^{N}) & 1\\ 1 & \cdots & 1 & 0 \end{bmatrix},$$
(13)

$$y = \begin{bmatrix} s^1 \\ \vdots \\ s^k \\ \lambda \end{bmatrix}, \quad d = \begin{bmatrix} 0 \\ \vdots \\ 0 \\ N \end{bmatrix}. \tag{14}$$

Again, we can use SVD to solve the above linear equation to find all the scale factors. Summing these scaled images generates a master image that eventually determines the final contrast performance optimized with the G-RDI.

The G-RDI algorithm we use for our reference-star-based optimization is different from the traditional RDI currently used by other groups. For the traditional RDI, a general PSF is reconstructed from the reference images, which is then used to subtract with each of the target images. This may induce a systematic error on the reconstructed PSF, because of the potential variations of the imaging system and the observational conditions such as the seeing condition and the airmass variations when the reference star is far away on the stellar position to that of the target star. On the other hand, each of the target images cannot be identical to one another. In our G-RDI, each of the target star images is optimized with all of the reference star images individually, and then the subtracted target images are further optimized by using the Lagrange multiplier method. Therefore, it provides a better subtraction to remove the speckle noise. Our G-RDI involves two steps of optimization, which is different from the LOCI used in the ADI-associated data reductions. Furthermore, all our reference and target stars are carefully chosen. That is, they must belong to the same stellar association and all these images must be taken at a time that is as close as possible in the same observational night, which can effectively mitigate this potential systematic error.

3 DATA REDUCTIONS WITH PALOMAR OBSERVATORY 200-INCH HALE TELESCOPE

3.1 Data collection

Our exoplanet imaging survey is a faint-start-oriented imaging program, with the goal to find low-mass companions. It will image hundreds of faint stars with an apparent magnitude $m_v = 7.5-15$ at the NIR K band. As the first observational run, it was conducted with the Palomar Observatory 200-inch Hale Telescope. In order to achieve high-resolution images, we used the PALM-3000 AO and the Palomar NIR camera Palomar High Angular Resolution Observer (PHARO), both standard facility equipment with the Hale Telescope.

The PALM-3000 AO wavefront sensor can be configured as 64×64 , 32×32 , or 8×8 pupil sampling modes to deliver good AO performance at the NIR bands for natural guide stars with different magnitudes at different seeing conditions. Details of the PALM-3000 AO system were discussed by Burruss et al. (2014) and Dekany et al. (2013). The Palomar Observatory has a general seeing condition on the order of 1.2–1.5 arcsec, and the PALM-3000 AO 32×32 and 8×8 can be effectively used to image faint star with an apparent magnitude $m_v = 10$ –14, at the NIR K band. For a star with a magnitude $m_v = 10$ and in the 32×32 mode, the AO

can deliver a moderate Strehl ratio of \sim 0.7, while with a magnitude $m_v = 13$ and in the 8 \times 8 mode it can deliver a Strehl ratio better than 0.4. This performance meets our observational requirements for faint stars with a magnitude between $m_v = 7.5$ and 14. The PHARO camera uses a Rockwell 1024 \times 1024 HgCdTe Astronomical Wide Area Infrared Imager (HAWAII) sensor, with a read noise <10 e $^-$. It is sensitive to the NIR J, H, and K bands, with an imaging scale of 0.040 or 0.025 arcsec pixel $^{-1}$. For our observation, we used the Palomar K-band filter with an imaging scale of 0.025 arcsec pixel $^{-1}$.

For our reference-star-based optimization, the data collection is a critical step. To achieve a good subtraction, both the target and reference stars must belong to the same stellar association, they must have similar celestial coordinates, and their images must be taken at a time as close as possible. We took images of over 20 stars from the Oh et al. (2017, hereafter Oh17) stellar association with the 200-inch Hale Telescope on a full night, of 2019 January 19. Dark-current and flat-field correction images were also taken subsequently after the imaging of the scientific target stars. From these target stars, we are able to pick up two stars images, with images of each star assigned to one group. For these two groups of images, one group is used as the target star, while the other is defined as the reference star. The reference star images are used to remove the speckle noise of the target star images according to the algorithm discussed in Section 2. It is worth noting that the target and reference stars must be selected from the same stellar association or cluster, so that they share similar spectra and (or) coordinates, which will allow good speckle subtraction. Because of this, they should have similar right ascension (RA) and declination (Dec.), so that the telescope does not need to move too much when it points from one star to the other, which ensures that the AO can deliver similar PSFs during this imaging process. All images were taken in the NIR K band, with a short exposure time depending on the magnitude of each star.

As a first demonstration, we pick up the HIP 72389 as the target star, and the TYC 3867-281-1 as the reference star. Both stars are members of the Oh17 stellar association. For all the images taken, we skip the first image in each group of images, because of the NIR camera's shutter defect issue. Dark images with the same exposure are subtracted. Flat-field correction is done on all images, taken with the 200-inch telescope dome calibration light source. Images in the same group are aligned by using a combination of both the 2D Gaussian function and the mass-centre methods. With these two methods, we first use the mass-centre method to find a rough centre position and then further use the 2D Gaussian function to find the fine position, since the Gaussian function is more accurate, it is sensitive to the background noise and thus is more intended to yield a wrong point if it is not well constrained.

For all the images taken during this observation, the intensities for the pixels located far away from the PSF peak are very low and are dominated by the background or camera readout noise, while at a close distance, speckle noise or diffraction pattern is dominant. Therefore, if we calculate the subtraction coefficients according to the whole image, the background noise would make the subtraction deviated from the optimization solution that we expect. Depending on the specific purposes, we need to use different regions to optimize for the subtraction coefficients. In the following sections, we use the HIP 72389 as the target star and the TYC 3867-281-1 as the reference star. In Table 1, we list the detailed information of these two stars. In addition, images of the TYC 3480-1209-1 from the same stellar association are also used as a reference star, as we will discuss in a later section. All these three stars have similar celestial coordinates and their images were taken consecutively, which facilitates speckle noise subtraction, as we discussed previously. One may note that

Table 1. Detailed information of target star and reference stars. For each star, 400 images are used.

Name	Group	RA	Dec.	m_v	Spectral type	Exp. time (s)	Start time (UTC)
HIP 72389	No.10 of Oh17	14 48 02.84	+56 09 33.14	10.02	G5	1.4	2019-01-20 12:52:00
TYC 3867-281-1	No.10 of Oh17	15 04 25.75	+59 52 50.82	9.62	K2	1.4	2019-01-20 11:08:19
TYC 3480-1209-1	No.10 of Oh17	14 53 04.83	+51 15 40.17	10.01	K2	1.4	2019-01-20 12:30:43

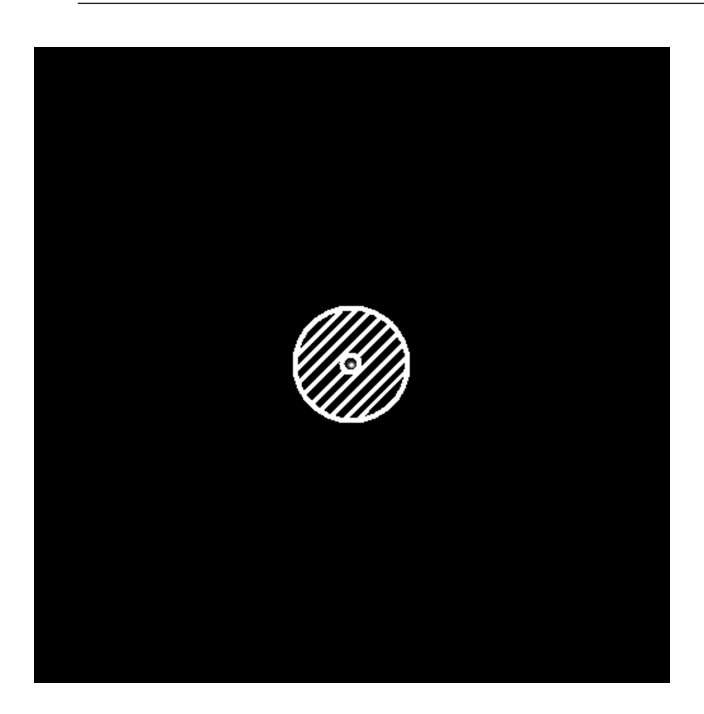


Figure 1. The selected optimized region for the annulus-region-based optimization.

TYC 3867-281-1 and TYC 3480-1209-1 have the same spectral type, which is different from that of the target star HIP 72389. This means that the subtraction between the two reference stars should deliver better contrast. Here we use the HIP 72389 as the target star and subtract it with a reference star of a different spectral type, because it has a low-mass companion candidate that is suitable for the demonstration.

To make sure that all pixel intensities in the used region outside the PSF mask are not saturated, we check all the raw data of the target star HIP 72389 and the reference stars TYC 3867-281-1 and TYC 3480-1209-1. We found that most of the raw data are not saturated at the PSF peak, except for a few that are saturated in 1 or 2 pixels. Because we use a mask to block out all image data in a circle within the $2\lambda/D$ radius around the PSF (where λ is the wavelength, and D is the telescope diameter), this ensures that all the data used in our calculations are unsaturated. To effectively subtract the speckle noise, here we propose the annulus-region-based and the local-annulus-region-based optimization techniques, respectively, which will be discussed in the following sections.

3.2 Single-annulus-region-based optimization

Speckles are the dominant noise that will impact the quality of the signal-to-noise ratio (SNR) for the exoplanet imaging, especially at a region that is close to the host star. Therefore, we can use a speckle-based region to effectively subtract the speckle noise. To effectively eliminate the speckles, we choose an annulus region that

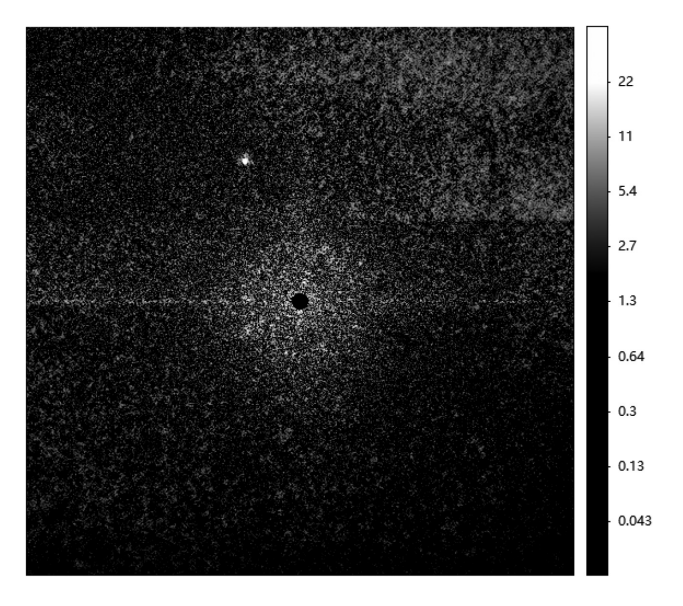


Figure 2. HIP 72389 system image reduced with the G-RDI, optimized in a single-annulus region.

is closely around the host star's PSF, as shown for the hatched area in Fig. 1. For this optimization, we choose the annulus width of $10\lambda/D$ as such that the annulus has a radius between $2\lambda/D$ and $12\lambda/D$. Here we use the 400 HIP 72389 images as that of the target star, and the 400 TYC 3867-281-1 images as that of the reference star. Once the optimization region is defined, we use 400 target images and 400 reference images to optimize for the speckle subtraction according to our G-RDI, and these two steps of optimization deliver a reduced target master image. Fig. 2 shows the target master image reduced with our G-RDI, optimized in a single-annulus region. The corresponding azimuthally averaged contrast for the reduced target star HIP 72389 is shown in Fig. 3. It is clear that at the IWA of $2\lambda/D$ and $5\lambda/D$, contrasts of 1.09×10^{-4} and 9.22×10^{-5} are achieved, respectively.

In addition to the G-RDI, we also calculate the contrast with the reference star subtraction using the LOCI algorithm discussed in Section 2, which only includes the first step of the optimization in the G-RDI. As we can see from Fig. 3, the LOCI-based reference star subtraction can deliver contrasts of 2.13×10^{-4} and 1.52×10^{-4} , at the IWA of $2\lambda/D$ and $5\lambda/D$, respectively. Therefore, our G-RDI can improve the contrast up to a factor of 2 better than that of the LOCI-algorithm-based RDI subtraction. In the remainder of this paper, we will only use the G-RDI to investigate our reference-star-based imaging performance.

3.3 Multiple-annulus-region-based optimization

The single-annulus-region-based optimization can be further improved, if we increase the number of annulus regions in such a way that each region corresponds to a small area to be optimized. Here, we

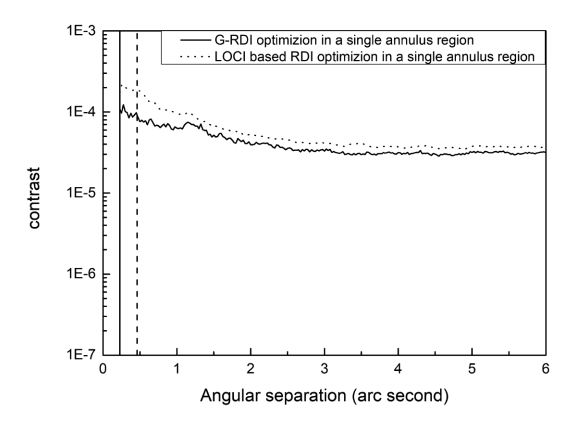


Figure 3. Azimuthally averaged contrast achieved with the G-RDI, optimized in a single-annulus region (solid line). For comparison, we also add the contrast optimized with the traditional LOCI algorithm (dot line). The solid and dashed vertical lines correspond to the $2\lambda/D$ and $5\lambda/D$ angular distances, respectively.

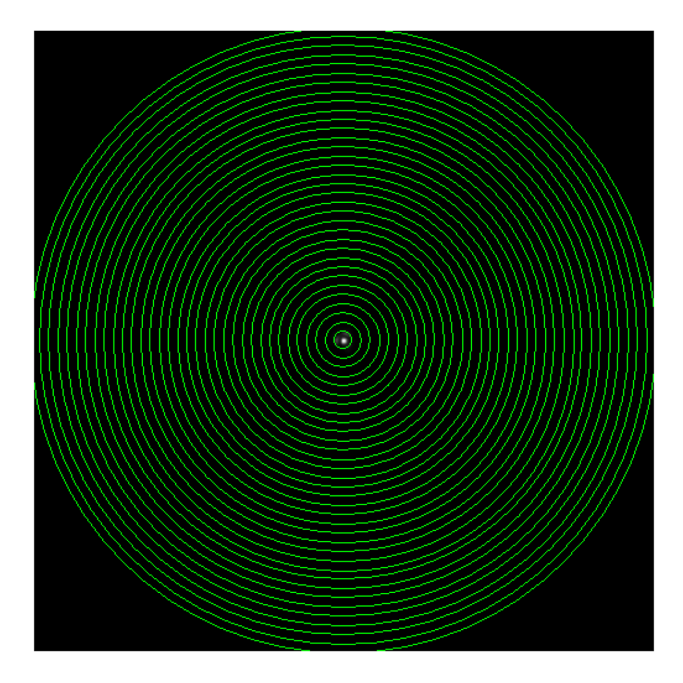


Figure 4. Definition of the multiple-annulus regions for the G-RDI. The width of each local region is equal to $1\lambda/D$ in the radial direction.

still use the HIP 72389 as the target star, and the TYC 3867-281-1 as the reference star, so that we have total 400 images for the target star and total 400 images for the reference star group. Fig. 4 shows how we define the multiple-annulus regions. We define each local region as a small annulus area with a width of $1\lambda/D$ in the radial direction, and then optimize for the speckle subtraction in this small region. The optimization is done one by one with the G-RDI, until it is completed over all the local annulus regions. Depending on the pixel number in each local annulus region, one may need to interpolate each image so that enough pixels in each annulus region are available for such an optimization. For our case, we interpolate each image to make it four times larger in each of the x and y directions. The left-hand panel of Fig. 5 shows the reduced master image of the HIP 72389. We can see from this figure that the local annulus region that hosts the low-mass companion may result in an undersubtraction because of the

contribution of the companion's intensity. This undersubtraction can be avoided by further re-optimizing this local region by applying a local mask to block out this companion in this region, with the result shown in the right-hand panel of Fig. 5, in which the undersubtraction is avoided and thus this local region has a similar intensity with its neighbourhood regions. The achieved azimuthally averaged contrast is shown in Fig. 6. As estimated, the use of the multiple regions can significantly improve the performance, and at the IWA of $2\lambda/D$ and $5\lambda/D$, contrasts of 5.49×10^{-5} and 3.46×10^{-5} are achieved, respectively.

3.4 Multiple-annulus-region-based optimization with two reference stars

In the previous section, we have demonstrated that using one reference star, our G-RDI can deliver excellent performance by using multiple-annulus regions. In fact, our G-RDI can deliver even better performance by using two reference stars. Again, we use the HIP 72389 as the target star, in which 400 images are used. For the reference stars, both TYC 3867-281-1 and TYC 3480-1209-1 are used, each with 400 images. Therefore, the reference star group has 800 images in total. Here, we use our G-RDI to optimize over the multiple-annulus regions. Fig. 7 shows the reduced master image of the target star HIP 72389. The corresponding azimuthally averaged contrast is shown in Fig. 8. For the optimization with two reference stars, contrasts of 9.36×10^{-6} and 7.96×10^{-6} are achieved at the IWA of $2\lambda/D$ and $5\lambda/D$, respectively. For comparison, we also include the G-RDI result with one reference star. We can see that for the optimization with two reference stars, the contrast can be improved by a factor of 2, over that with one reference star only. We also use the two reference stars, in which each with 200 images only to calculate the contrast, and we found that both using different stars and increasing the reference star image number can contribute to the improvement of the contrast performance in our G-RDI. These results further confirm that the two reference stars optimization can indeed improve the contrast performance for exoplanet imaging.

For the G-RDI imaging, long exposures are not limited by random, short-lived atmospheric speckles, but by quasi-static speckles, which may be introduced by the telescope and imaging optics. Statistical tools to assess the significance of a point source detection at large angles are most often based on the assumption that the underlying noise is Gaussian. However, it was noticed recently that the speckle noise in raw high-contrast images is never Gaussian when the static or quasistatic aberration is presented in the imaging system. In this case, the probability density function (PDF) of speckles in raw images does not follow a well-behaved normal (i.e. Gaussian) distribution, and is better described by a modified Rician (MR) distribution. This may introduce false signal for the exoplanet imaging at small angular separation and may require a detection threshold up to several times higher to achieve a confidence level equivalent to that at 5σ for a Gaussian noise distribution (Marois et al. 2008b; Mawet et al. 2014). A good data reduction method should be able to effectively suppress this static or quasi-static wavefront-error-induced speckle noise. In this regard, we also calculate the discrete pixel intensity distribution. Fig. 9 shows the histograms of the pixel intensity distribution before (left-hand panel) and after (right-hand panel) the two-reference-star G-RDI subtraction, respectively. The statistics of the residual noise is calculated between the $2\lambda/D$ and $5\lambda/D$ region. We can see that while the raw image, which is the sum of 400 short-exposure images, indeed follows a MR distribution, the pixel intensities of the G-RDI reduced image obey a Gaussian distribution very well. This result

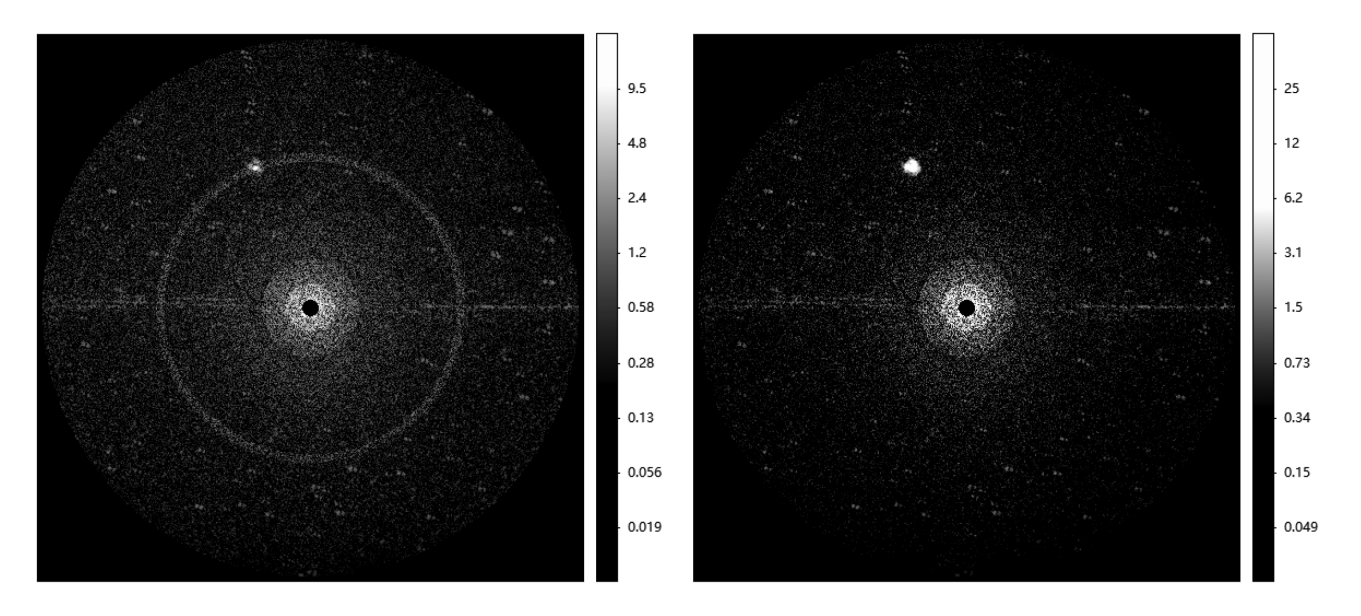


Figure 5. HIP 72389 system image reduced with the G-RDI in the multiple-annulus regions with one reference star. Left: no exoplanet mask used. Right: with exoplanet mask used.

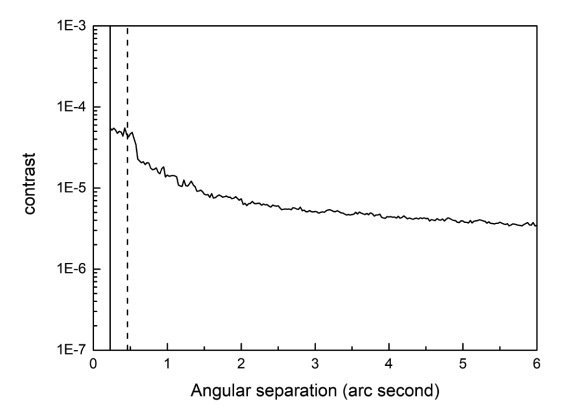


Figure 6. Azimuthally averaged contrast achieved with the G-RDI in the multiple-annulus regions with one reference star. The solid and dashed vertical lines correspond to the $2\lambda/D$ and $5\lambda/D$ angular distances, respectively.

indicates that the static and quasi-static speckles are at a significantly low level after the G-RDI subtraction

4 COMPARISON WITH OTHER DATA REDUCTION METHODS

IRS (Ren et al. 2012) is a high-contrast image reduction technique that uses the star PSF for self-subtraction, i.e. the star image is subtracted with its 180° rotated PSF. If the speckle-associated wavefront error is expressed as a Taylor series of different orders, consisting of both even and odd orders, the IRS subtraction will remove all the even terms of the speckle noise, leaving the odd terms only unsubtracted. The odd terms of speckle noise can be further suppressed, if a coronagraph is used for the imaging.

OIRS (Dou et al. 2015) provides an improvement over the IRS. OIRS divides the entire image area into several small regions. In each small region, OIRS uses the IRS 180° rotated image as the reference image to optimize for the subtraction, and thus to remove

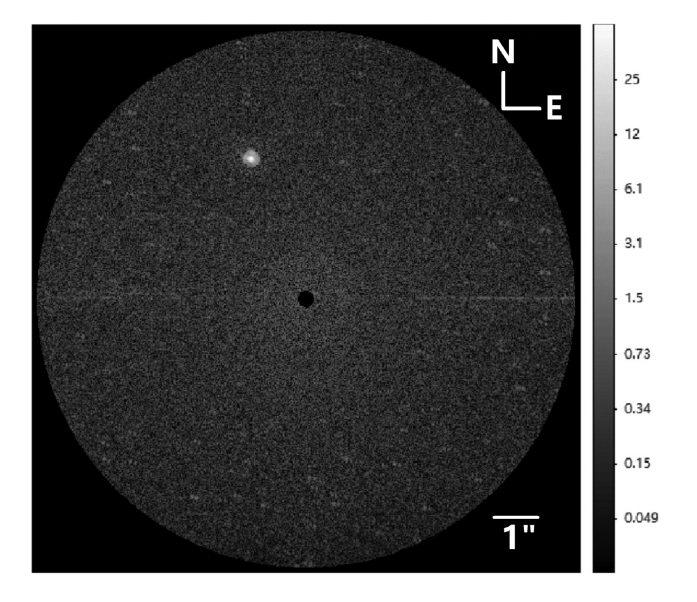


Figure 7. HIP 72389 system image reduced with the G-RDI in multipleannulus regions with two reference stars.

the speckle noise. OIRS can be used for both the alt-azimuth and equatorial mount telescopes.

PYNPOINT (Amara & Quanz 2012) is a high-contrast image reduction technique based on the PCA. PYNPOINT uses the basis function of orthogonal complete basis sets derived from the PCA to construct the reference PSF, which is then used to subtract with each of the target images. PYNPOINT typically uses 100 PCA coefficients, since further increasing the coefficient number has no significant improvement on the performance. PYNPOINT was originally developed for exoplanet image data reduction with the alt-azimuth mount telescope. For the alt-azimuth telescope, the reference images and the target images are taken from the same target star, and the exoplanet flux will not be subtracted out, because companion images rotate as a function of time but speckles do not. However, for equatorial mount telescope, since

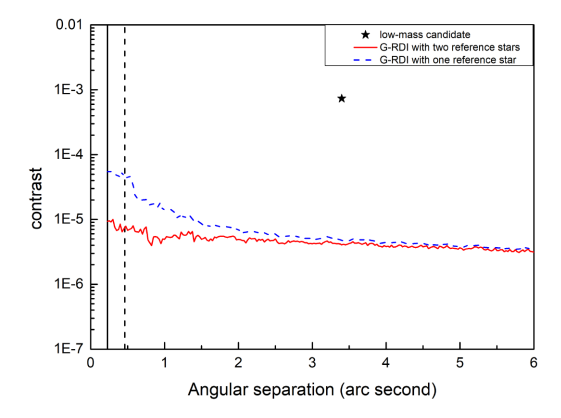


Figure 8. Azimuthally averaged contrasts achieved with the G-RDI in multiple-annulus regions with one (dashed line) and two (solid line) reference stars, respectively. The asterisk indicates the contrast of the companion. The solid and dashed vertical lines correspond to the $2\lambda/D$ and $5\lambda/D$ angular distances, respectively.

there is no image rotation, to avoid the subtraction of the exoplanet flux the reference images could not be selected from the same target star. Here, we use one star as the reference star to construct the PCA basic functions, and then find the coefficients of the basic functions by optimizing the subtraction between the target star image and the reference images during each fit for the speckle noise subtraction for each target star image. Because PYNPOINT needs to mask the centric portion before getting a basis function, we mask the central region for all the images, including both the target images and reference images. A circular region with a radius of $2\lambda/D$ is used as the mask to block the PSF central region. Such a technique is, in fact, used by the RDI technique for the current coronagraphic imaging with the Keck telescope (Xuan et al. 2018).

In addition to using the RDI, we also use the RDI combined with the reference star frame selection approach. As discussed above, PYNPOINT is a PCA-based ADI technique. Ruane et al. (2019) used the PCA-based method in their RDI, without the tight restriction as adopted in the reference star selection. That is, their reference stars are not bundled to be a member of the same stellar association with that of the target star. In that situation, they found that the reference star frame selection is critical to deliver a good performance. They assigned a score to each reference frame using three metrics: the mean square error (MSE), the Pearson correlation coefficient (PCC), and the structural similarity index metric (SSIM). Of the three frame selection approaches, it was found that the SSIM delivers the best performance. It will be interesting to see how the performance of PCA-based RDI, combined with the SSIM frame selection technique, can be improved when it is applied to our target and reference stars. Here, for comparison, we also use this RDI combined with the SSIM frame section technique to reduce our data, in which 30 per cent of the reference frame was rejected, the same with that adopted by Ruane et al. (2019).

Fig. 10 shows the results reduced from the 400 images of the target star HIP 72389, with the IRS, OIRS, and RDI, respectively, with the corresponding contrasts shown in Fig. 11, in which the 400 images of the star TYC 3867-281-1 are used for the reference star. In addition to the RDI, RDI combined with the SSIM frame selection is also shown in Fig. 11. The results of these methods show strong speckles in the IWA area, where it is much stronger than the annulus-region-based and the local-annulus-region-based optimization techniques we proposed. Spider-induced noise is still dominant and has not been effectively removed. From Fig. 11, we can see that the RDI

delivers better contrast at a small angular distance such as at the $2\lambda/D-10\lambda/D$, while the OIRS provides better performance at a large angular distance. We can also see that the RDI combined with the frame selection technique delivers almost the same performance as the one without frame selection, indicating that our stellar association target selection is an effective strategy, for which no frame selection is needed. Therefore, in the remaining part of this paper, we will only use the RDI to compare with our proposed techniques.

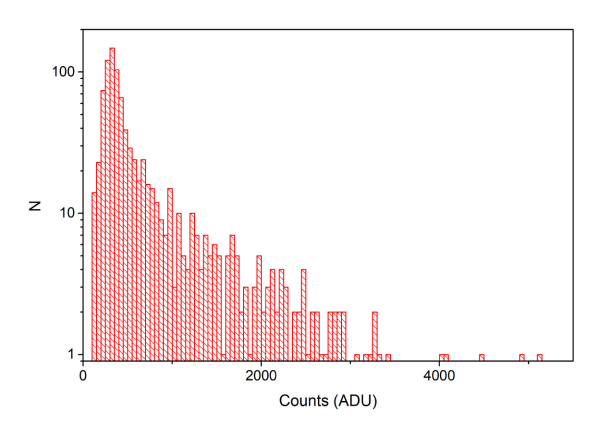
Since we only use 400 images for each target star, it will be helpful to see the contrast preference of our data reduction techniques, by comparing it with that of the photon noise limited case that defines the best performance a system can actually deliver. The photon noise converted from the intensity count number can be calculated as

$$\sigma = \sqrt{N/(n \times G)},\tag{15}$$

where n is the total image number used in the data reduction. For our observations, 400 images are used for each target star, thus we have n = 400. N is the intensity count number in the final master image that is the average of the n reduced images. G is an inversegain factor in the unit of e⁻/DN, which converts the intensity count number to the photon-electron, where DN is the so-called data number in the intensity count. The PHARO camera we used for the data collection is based on a Rockwell 1024 × 1024 HAWAII HgCdTe chip with an inverse gain of 3.6 e⁻/DN. In Fig. 12, we show the azimuthally averaged contrasts of the target star HIP 72389 achieved with different data reduction techniques, together with the photon noise limited case. The photon noise limited contrast is calculated in a small angular separation up to 2 arcsec where the speckle and phonon noise are dominant. The G-RDIs with one and two reference stars are calculated with the approaches optimized for the speckle noise subtraction discussed in the previous section, in which 400 and 800 extra reference star images are used with the 400 target images, respectively. We can see that among all the data reduction techniques presented here our G-RDI with two reference stars delivers the best contrast, and photon noise limited performance is achieved, indicating that both the dynamic and quasistatic speckles are well suppressed. Compared with the traditional RDI, our G-RDI significantly improves the contrast performance by up to 20 times, in the IWA between $2\lambda/D$ and $5\lambda/D$.

5 OBSERVATIONAL RESULTS OF OTHER LOW-MASS CANDIDATES

In the same observational night, we conducted the observation of over 18 target stars in total, each with 400 images. Including the HIP 72389 star system, we found eight low-mass candidates in five star systems, which have a contrast between 10^{-3} and 10^{-5} . We noted that the low-mass companion recently discovered by Bowler et al. (2017) has a contrast between 1.3×10^{-3} and 7.3×10^{-5} with its host star. We thus set the 10^{-3} contrast as a threshold for our exoplanet imaging survey. That is, if the contrast of the companion is equal to or smaller than 10^{-3} , it is viewed as a low-mass candidate, which may be a faint dwarf or an exoplanet, depending on further photometric characterization. In Table 2, we list all these star systems that may host low-mass companions. For five host stars, we find that they have eight low-mass candidates. For these target stars, we use our G-RDI in multiple-annulus regions with one reference star to reduce these images, with the resulted master images shown in Figs 13–16, respectively. For clarification, each low-mass candidate is enclosed with a small circle in these figures. The host star HIP 72389 is reduced with two reference stars as we discussed previously, with the associated image shown in Fig. 7. The TYC 3698-475-1 and



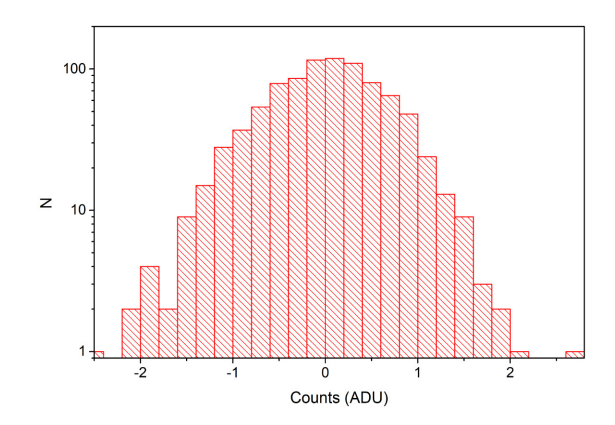


Figure 9. Histograms of pixel intensity values before (left-hand panel) and after (right-hand panel) the two-reference-star G-RDI subtraction. The statistics of the residual noise is calculated in a region between the $2\lambda/D$ and $5\lambda/D$ angular separation, with the pixel number N shown on a logarithmic scale.

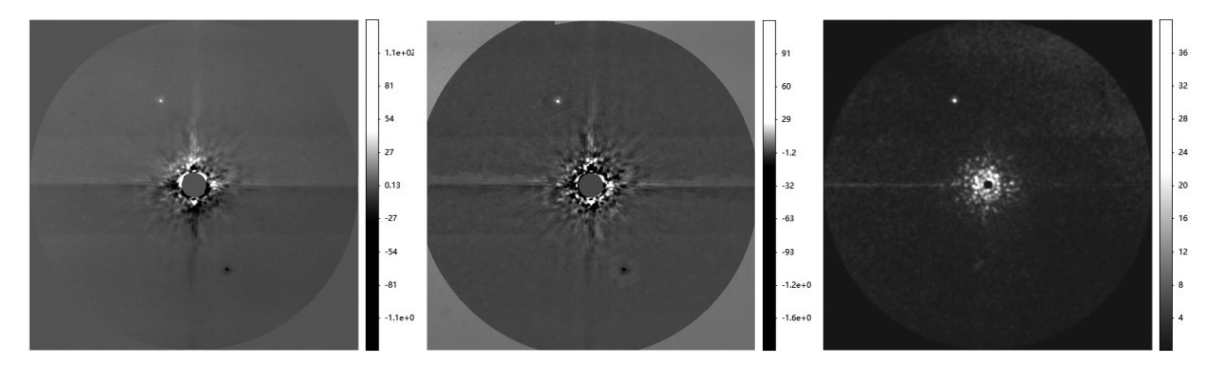


Figure 10. The HIP 72389 reduced images with three different methods. Left: reduced image with the IRS with a central mask of $5\lambda/D$. Middle: reduced image with the OIRS with a central mask of $5\lambda/D$. Right: reduced image with the RDI with a central mask of $2\lambda/D$.

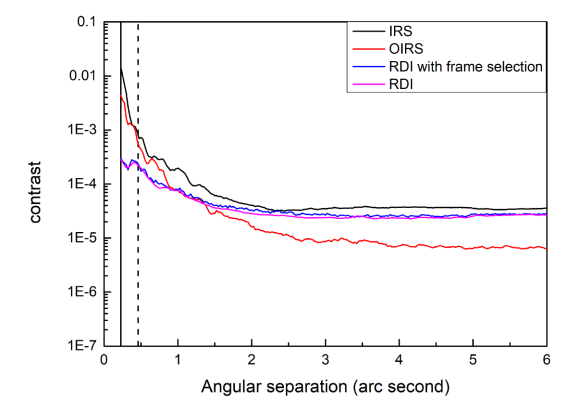


Figure 11. Azimuthally averaged contrasts achieved with the IRS, OIRS, RDI, and RDI with frame selection, respectively. The solid and dashed vertical lines correspond to the $2\lambda/D$ and $5\lambda/D$ angular distances, respectively.

TYC 3715-701-1 have two and three potential low-mass candidates, respectively, with different brightnesses. These candidates stand out from the background noise, with an SNR better than 6 to the local background. It is worth noting that for the TYC 3698-475-1 system the innermost one can only be seen from the image reduced with our G-RDI, and it would be buried in the speckle noise if the images were reduced with other data reduction techniques. The imaging of 18 target stars and the discovery of a large number of low-mass candidates in only one night of the observation using a 5-m class telescope at a site with a moderate seeing condition clearly

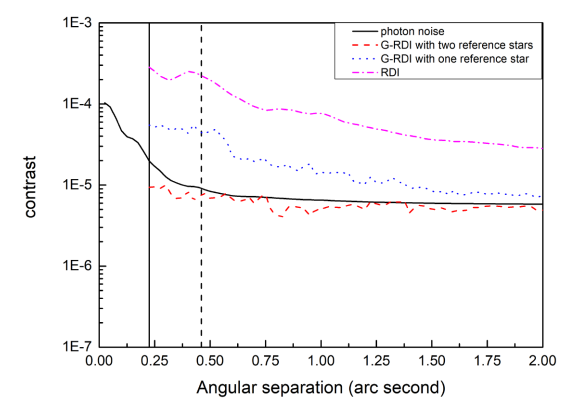


Figure 12. Photon noise limited contrast (solid line) compared with that achieved with the traditional RDI (dash–dotted line) and our G-RDIs with one (dotted line) and two (dashed line) reference stars. The solid and dashed vertical lines correspond to the $2\lambda/D$ and $5\lambda/D$ angular distances, respectively. The RDI and G-RDI contrasts are calculated according to the approaches discussed in the previous section.

demonstrate the high observational efficiency and high performance offered by the G-RDI method.

Indeed, there are some limitations for current ADI-associated data reduction techniques that rely on field rotation for the speckle noise subtraction, as discussed in detail by Ruane et al. (2019). These include the timing constraints, since ADI observations must be carried out during a relatively narrow time window to achieve an

Table 2. Details of the star systems that may host low-mass candidates. 400 images were took for each target star.

Host star name	m_k of host star	Age (Myr)	Star-companion distance (arcsec)	Exposure time (s)	Magnitude difference
HIP 11156	7.7		5.93	1.4	~8.391
HIP 72389	8.113	~750	3.33	1.4	~7.89
TYC 3698-475-1	7.509		4.62/0.64	1.4	~7.879/~7.15
TYC 3715-701-1	7.759	< 750	5.02/5.6/4.22	1.4	~7.603/~10.56/~10.49
TYC 4049-648-1	7.665	< 750	7.58	1.4	~7.04

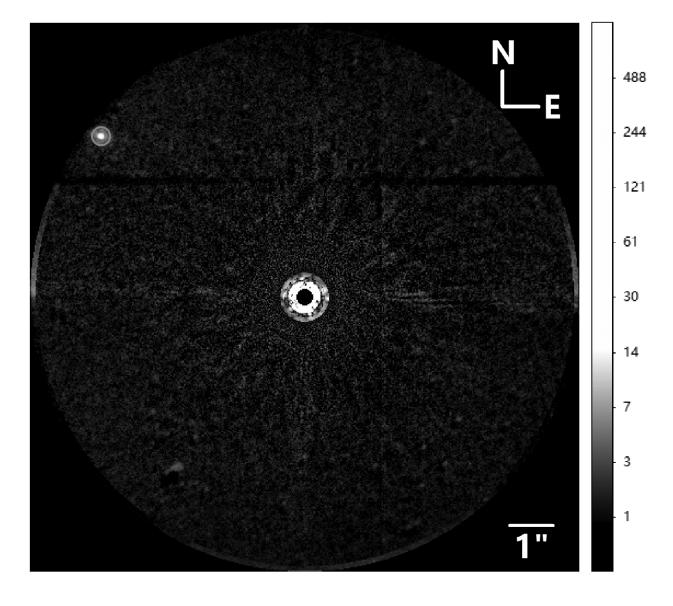


Figure 13. Image of the HIP 11156 system, reduced with the G-RDI in the multiple-annulus regions.

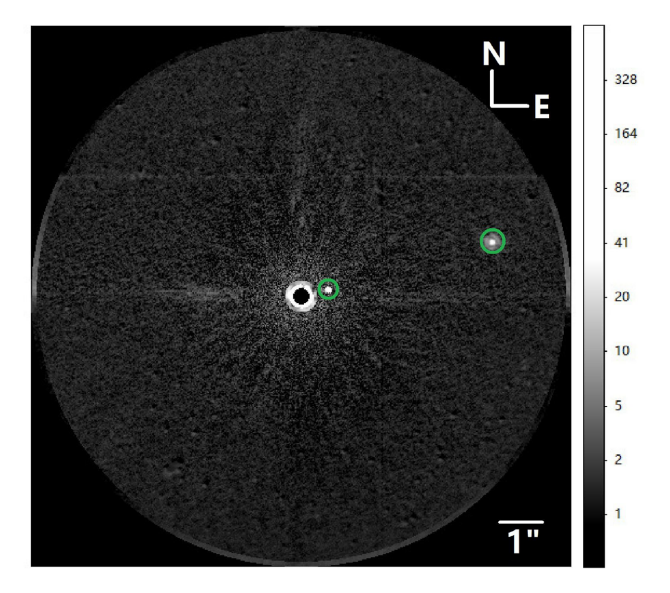


Figure 14. Image of the TYC 3698-475-1 system, reduced with the G-RDI in the multiple-annulus regions. Two low-mass candidates are revealed. One in a small IWA and the other in a large angular separation.

image rotation needed to avoid self-subtraction effects. They also suffer from the limited effective IWA, because of self-subtraction effects at small angular separations. In addition, the limited sky coverage suitable for the ADI self-image subtraction is also a limited

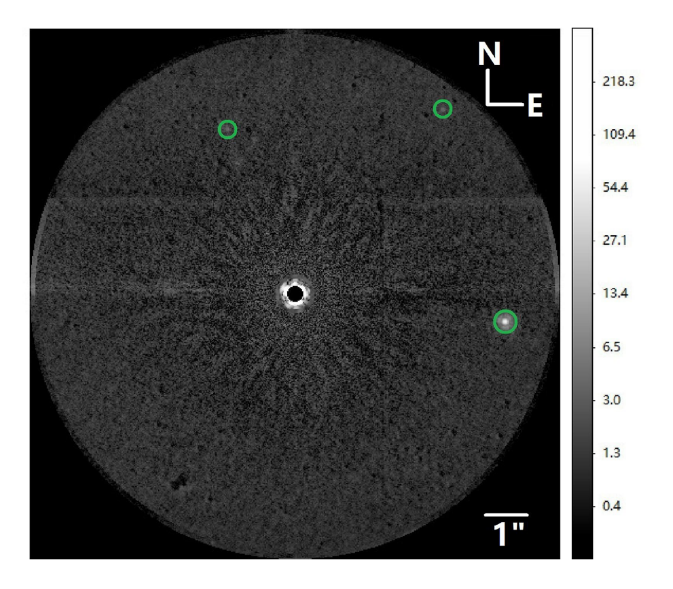


Figure 15. Image of the TYC 3715-701-1 system, reduced with the G-RDI in the multiple-annulus regions. Three low-mass candidates with different brightnesses are revealed.

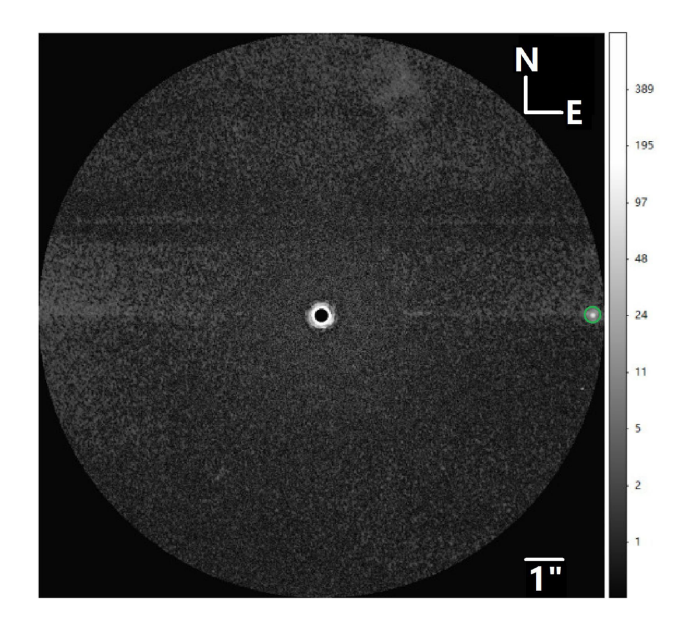


Figure 16. Image of the TYC 4049-648-1 system, reduced with the G-RDI in the multiple-annulus regions.

issue. All of these make the ADI-associated techniques not suitable for the high-efficient and high-contrast exoplanet imaging surveys at a small IWA distance, as we proposed in this paper.

2168 D. Ren and Y. Chen

To rule out that these candidates are not background objects, we will need to conduct subsequent proper-motion confirmation observations. Photometric measurements are also needed to further characterize the companion's physical properties. For the low-mass candidates we discussed in this section, except for the innermost one in the TYC 3698-475-1 system, they can be revealed by simply summing their short-exposure images, since they are relatively far away to their stars. It is possible that a candidate at a large angular operation such as that in the TYC 4049-648-1 system is a background star. However, for a contrast lower than 10^{-3} the possibility of a background object appears on a small field of view such as $1 \times 1 \times 10^{-2}$ is very low (Quanz et al. 2013).

6 EXOPLANET FLUX MEASUREMENTS

It is well known that ADI (Marois et al. 2006) associated techniques, such as the PYNPOINT (Amara & Quanz 2012) and LOCI (Lafreniere et al. 2007), suffer from the so-called exoplanet flux loss, because of the nature of the image-rotation-associated subtraction. This exoplanet flux loss depends on the angular distance to the host star, the brightness of the companion itself, and the parameters chosen in the specific method. Such a flux loss is more serious at a close angular distance, since the linear shift distance of the exoplanet image is proportional to its angular distance. This makes accurate photometric analysis difficult. Furthermore, the flux loss implies that long observational time is needed for the faint companion imaging, which reduces telescope observational efficiency.

Amara & Quanz (2012) used both LOCI and PYNPOINT to calculate the exoplanet flux in an IWA between $3\lambda/D$ and $5\lambda/D$. They found that LOCI underestimates the exoplanet close to a factor of 5, while the PYNPOINT underestimates it by a factor of 2. It will be interesting to investigate the possible exoplanet flux loss issue in our reference-star-based optimization. To calculate the exoplanet flux, we consider two cases. In case 1, no exoplanet mask is applied to block the exoplanet, and in case 2 an exoplanet mask is used in our data reduction as we discussed previously.

We inject one artificial exoplanet at an IWA of $2.5\lambda/D$, $3.5\lambda/D$, $4.5\lambda/D$, and $5.5\lambda/D$ individually, and evaluate how the exoplanet flux is changed in each of these angular distances. We use an intensity-scaled star PSF as an injected exoplanet. We calculate the average intensity at the full width at half-maximum (FWHM) of the injected PSF, and then use it to calculate the SNR. Exoplanet flux corresponding to five different intensities of 5σ , 10σ , 50σ , 100σ , and 1000σ is used, respectively. Since each Airy disc has about 45 pixels, we can directly calculate the noise σ at each exoplanet location over an area of the Airy disc. The injected exoplanet is scaled accordingly and added to the target images during the data reduction. Fig. 17 shows the reduced images at different combinations, with a mask applied to block the exoplanet in both the target and reference images, respectively, in which our multiple-annulus-region-based optimization (with one reference star) is used. In addition, we also calculate the flux in the case without the mask applied. The flux calculation results with and without exoplanet mask are listed in Table 3, in which the values with and without (in parentheses) mask are presented in percentage by comparing to the original fluxes. We can see that compared with the original flux, for the results without masks, the observed exoplanet fluxes indeed will have some change, reducing to 19.9 per cent of the original flux at a small IWA of $2.5\lambda/D$, while the results with masks almost have no change or the change only occurs when the SNR has a low value such as $\sigma = 5$. For our data reduction with mask, when the exoplanet image has a small SNR, the observed exoplanet flux may have a

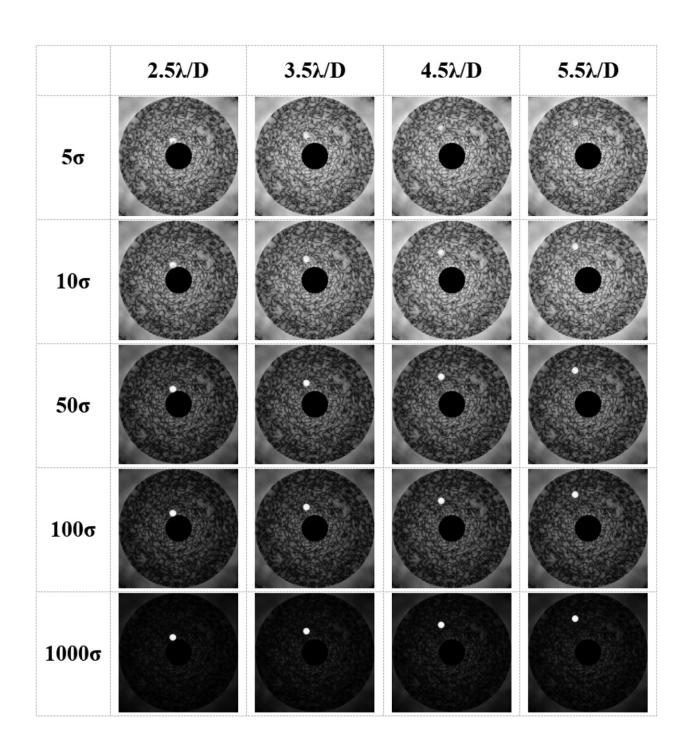


Figure 17. Injected artificial exoplanets at different SNR and IWA combinations.

Table 3. Measured flux of the artificial planets with and without mask (in parenthesis).

SNR	2.5λ/D	3.5λ/D	4.5λ/D	5.5λ/D
5σ	117.1 (19.9)	123.9 (21.2)	98.2 (23.5)	97.8 (25.0)
10σ	108.6 (15.0)	112.0 (22.1)	99.1 (25.4)	98.9 (28.6)
50σ	101.7 (16.3)	102.4 (23.4)	99.9 (27.8)	99.8 (29.5)
100σ	100.8 (16.7)	101.2 (23.2)	99.9 (28.5)	99.9 (30.0)
1000σ	100.1 (17.1)	100.1 (22.7)	100.0 (28.4)	100.0 (30.4)

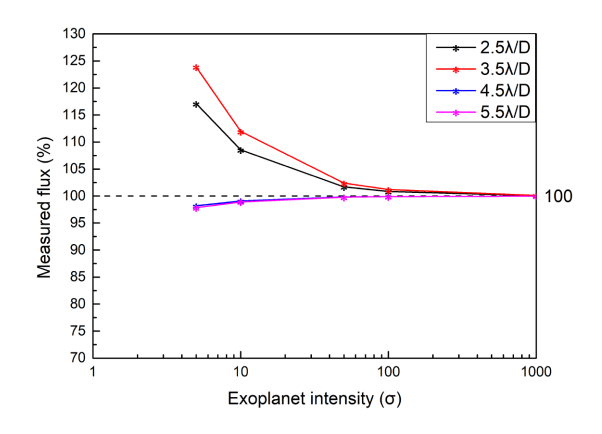


Figure 18. Retrieved precision of the measured exoplanet flux versus original injected flux with exoplanet mask applied, at different exoplanet intensity.

little change, but this change is on the local noise level, i.e. this change is dominated by the local noise, not by our data reduction method. When the exoplanet image has a large SNR, the observed flux has no change. The retrieved precision of the measured exoplanet flux corresponding to different exoplanet intensity, reduced with the annulus region optimization technique with mask is shown in Fig. 18 in percentage, which indicates that when the exoplanet SNR

increases, the retrieved flux converges to a precision of 100 per cent. The above results clearly indicate that no exoplanet flux change is induced by our data reduction method if an exoplanet mask is used.

7 PERFORMANCE LIMITATION

Speckle noises play a dominant role in exoplanet imaging. There are two types of speckle noise and their behaviours are fundamentally different. Therefore, they must be handled differently. The dynamic speckle noise varies randomly as a function of time, and thus can be effectively suppressed by increasing the effective exposure time in imaging (Marois et al. 2006). That is, by increasing the short exposure image number N, it could be suppressed until the speckles are dominated by the static or quasi-static noise. For the G-RDI and RDI, the static speckles can be totally subtracted, and thus will not be considered here. For ground-based observations, extreme adaptive optics (ExAO) is a powerful tool for exoplanet imaging. For AO imaging, the incoming wavefront is corrected by a deformable mirror (DM), whose actuators determine the residual speckle noise distribution. The benefits of ExAO exoplanet imaging are twofold. The ExAO corrects the incoming wavefront by pushing most of the light into the PSF Airy disc, which is proportional to the Strehl ratio S, and provides the so-called diffraction-limited imaging. On the other hand, the ExAO pushes the residual noise into a large area that is a function of the actuator number, which further reduces the intensity of the speckle noise.

For an AO system, the major dynamic errors include photon noise, readout noise, and limited bandwidth correction error. For the G-RDI, the photon noise in the AO wavefront sensing may be the dominant source in the dynamic speckle noise. For reference star differential imaging, the target and the reference stars may have different stellar magnitudes. This magnitude-variation-induced speckles between the target and reference stars in our G-RDI are viewed as a dynamic speckle noise, since this noise randomly changes around a static error, from one image to the other. Even though this error-induced speckle noise can be suppressed by summing large reduced images, it does reduce the contrast for a specific image number. Stellar-magnitude-variation-induced dynamic speckle noise can be suppressed by several methods. One can select bright stars for imaging so that the AO has enough photons for wavefront sensing, and in this case, the AO performance will be stable even though the guide star magnitude has some variation. This method can only be applied to bright targets; on the other hand, we can select target and reference stars that have similar stellar magnitudes. In our observations, our target and reference stars used in the G-RDI have a magnitude difference of 1–2, which ensures that photon noise limited contrast is achievable, as we demonstrated in the previous sections.

For an ExAO system with a Strehl ratio S and a DM with $N \times N$ actuators, the ExAO corrected speckle noise is distributed in an area that is a function of the actuator number, and the normalized intensity of the residual noise can be approximately calculated as $(1 - S)/N^2$ (Serabyn et al. 2007). For our G-RDI, by summing a large number of short-exposure images, we achieve photon noise limited performance, which indicates that we can continue to increase the image number until the quasi-static noise becomes dominant. The AO-compensated long-exposure PSF of the primary star can be modelled as the sum of a diffraction-limited core and a residual halo (Racine et al. 1999). For our G-RDI, the diffraction-limited core can be totally subtracted, leaving the residual halo that is determined by the quasi-static wavefront error, the critical factor that eventually limits the performance for the G-RDI subtraction. Since our concern is only the wavefront difference for the G-RDI

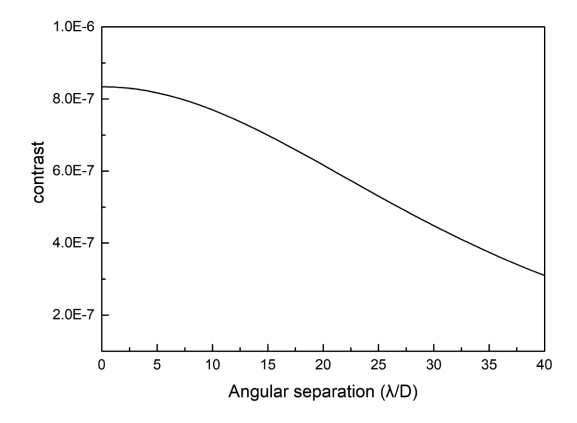


Figure 19. AO quasi-static wavefront error variation determined contrast.

two-star subtraction, for the quasi-static wavefront error sensitivity analysis we can assume that one star has a perfect wavefront, while the other one has a relative wavefront error that is determined by the quasi-static wavefront difference. For a Strehl ratio S' that is determined by the slow variation of the AO quasi-static wavefront error, the associated residual halo contains a fraction of (1-S') flux that cannot be subtracted by our G-RDI. According to Racine et al. (1999), a convenient Moffat profile with an index of 11/6 and unit volume can be used for the numerical calculation of this shape function. Therefore, the contrast floor that is eventually determined by the AO quasi-static wavefront error is

$$I_{\text{static}}(\theta) = (1 - S') \frac{0.488}{\omega^2} \left[1 + \frac{11}{6} \left(\frac{\theta}{\omega} \right)^2 \right]^{(-11/6)},$$
 (16)

where S' is the variation of the Strehl ratio between the target and the reference stars, because of the quasi-static wavefront error occurred in the AO system during the observation of the target and reference stars. ω is FWHM of the residual halo that contains 25 per cent of its flux. θ is the angular separation from the host star PSF central peak. For the Palomar AO system with 64×64 actuator sampling the 200-inch telescope pupil, we have $\omega = 64 \times \lambda/D$, in which λ and D are the working wavelength and telescope aperture, respectively. For convenience, we use the λ/D as the unit for both ω and θ parameters.

The quasi-static Strehl ratio variation may be induced by the thermal variation, possible air flow, and mechanical distortion on the AO imaging optical path. For a quasi-static phase error $\Delta\phi$, the corresponding Strehl ratio can be calculated as $S'=\exp(-(\Delta\phi)^2)$. The PALM-3000 has a 30-nm absolute static calibration error (Dekany et al. 2013). We use this absolute error as the quasi-static wavefront variation and of course this may result in a conservative performance estimation. The 30-nm static error corresponds to a Strehl ratio of 0.993, in the case of quasi-static wavefront error limit. In Fig. 19, we plot the AO quasi-static wavefront error variation determined contrast. As we can see, for an angular separation from 0 to $10\lambda/D$, the quasi-static wavefront-variation-induced speckle noise sets a contrast floor to a value between 8.34×10^{-7} and 7.70×10^{-7} between the angular separation 0 and 5 λ/D , respectively, and it will be further reduced at a larger IWA.

The PALM-3000, with 64×64 active actuators, is an ExAO imaging system designed for 10^{-7} contrast exoplanet imaging (Dekany et al. 2013). It is located on a compact and rigid optical bench enclosed in an individual structure in the telescope Cassegrain cage, which makes the system extremely stable to reduce the quasistatic speckle noise variation during an observational run. The large actuator number of the PALM-3000 and the stable system can

effectively suppress both the quasi-static and dynamic noises, which makes it suitable for our reference star differential imaging. It is notable that previous exoplanet imaging observations with the Hale PALM-3000 only achieved a contrast not better than 8×10^{-6} . The instrument of the project 1640 (Oppenheimer et al. 2012) can only achieved an observational contrast on the speckle floor on the order of 1×10^{-5} with bright targets in the H band (Oppenheimer et al. 2013; Pueyo et al. 2015), although a contrast of 10^{-7} is achievable in the laboratory test. Using the PALM-3000 and Hale Telescope with a small aperture size with an equivalent aperture of 1.5 m, Serabyn et al. (2010) achieved a contrast around 5×10^{-6} in the K-band imaging, which is within a factor of 2 that given by the photon statistics noise. The actual performance is determined by a number of factors, such as the observational seeing condition, AO performance, observational wavelength, extra dedicated instrument, and data reduction algorithm used to remove the speckle noise. In fact, the photon statistics noise defines the ultimate performance that a system can achieve. In the previous section, we have showed that using 400 target star images, we have achieved a contrast of 2.0×10^{-5} and 9.3×10^{-6} at the angular separation of $2\lambda/D$ and $5\lambda/D$, respectively, in the photon noise limited case. If we assume 4 h are the maximum equivalent and effective exposure time, this implies an ultimate contrast of 4.0×10^{-6} and 1.9×10^{-6} , respectively. Considering these highcontrast imaging observations conducted with the Hale PALM-3000, it is obvious that their performances are speckle noise limited at a small IWA separation, which reflects the need to develop a robust data reduction technique to achieve this ultimate performance, and this also applies to current exoplanet imaging programs with 8-m class telescopes that have not yet achieved the design or photon noise limited performance (Vigan et al. 2015).

8 CONCLUSION

High-contrast imaging at a small IWA distance and high observational efficiency are two critical issues that limit the discovery for exoplanet imaging surveys. Reference-star-based subtraction or the RDI-associated techniques have the potential to provide better contrast at a small IWA than that of the widely used ADI-associated data reductions. Fully exploring this approach will provide new opportunities for exoplanetary discovery that current techniques could not offer. We developed a reference-star-based optimization approach called G-RDI, which is dedicated to exoplanet highcontrast imaging survey at a small IWA with high observational efficiency. Compared with the traditional RDI, a unique feature for our data reduction approach is that it uses scientific target stars in the same stellar association as the reference star to optimize for speckle noise subtraction, and does not need extra time to image a reference star that was widely used in the traditional RDI. An inherent issue for the widely used ADI-associated data reductions is the subtraction of the exoplanet flux at a small IWA, since the image self-subtraction with the use of the field rotation. By using an exoplanet mask, our G-RDI can totally avoid the exoplanet flux subtraction during the data reduction. Our G-RDI algorithm is based on the least-square method, which involves two steps of optimization for maximum speckle noise subtraction and thus offers better performance. Our G-RDI can be used to subtract speckle noise via the optimization in a single- or multiple-annulus regions. We further proposed, for the first time, the use of multiple guide stars, and demonstrated that our G-RDI, combined with two reference stars, can provide excellent contrast at a small IWA, much better than that offered by current exoplanet imaging data reduction techniques. With only 400 images of a target star, each image with an exposure of 1.4 s, a contrast of 9.36×10^{-6}

 7.96×10^{-6} at a small IWA of $2\lambda/D$ – $5\lambda/D$ is achieved with the G-RDI, which significantly improves the contrast performance by up to 20 times over the current RDI techniques.

Using the Palomar Observatory 200-inch Hale Telescope, we demonstrated that our reference-star-based optimization techniques can be effectively used for exoplanet survey with ExAO, where a large amount of DM actuators are deployed. In an observational run of one night only, we successfully imaged 18 star systems. This work demonstrated the high efficiency of the G-RDI and its potential for exoplanet high-contrast imaging. Even though our reference-star-based optimization discussed here is originally proposed for equatorial mount telescopes, it can also be used for the alt-azimuth mount telescopes, where field rotation is available.

ACKNOWLEDGEMENTS

We thank the anonymous referee for detailed and valuable comments on our manuscript, which significantly improves the quality of this paper. Jonathan Fernandez read through the manuscript and provided corrections. DR acknowledges the supports from the National Science Foundation (NSF) under the grants AST-1607921 and AST-1906166, and a grant from the Mt. Cuba Astronomical Foundation. This observation was made possible by the Telescope Access Program (TAP).

DATA AVAILABILITY

The data underlying this paper will be shared on reasonable request to the corresponding author.

REFERENCES

Amara A., Quanz S. P., 2012, MNRAS, 427, 948

Amara A., Quanz S. P., Akeret J., 2015, Astron. Comput., 10, 107

Beuzit J.-L. et al., 2008, Proc. SPIE, 7014, 701418

Bloemhof E. E., 2004, in Gonglewski J. D., Gruneisen M. T., Giles M. K., eds, Proc. SPIE Vol. 5553, Advanced Wavefront Control: Methods, Devices, and Applications II. SPIE, Bellingham, p. 281

Bonnefoy M. et al., 2011, A&A, 528, L15

Bowler B. P., 2016, PASP, 128, 102001

Bowler B. P., Nielsen E. L., 2018, in Deeg H., Belmonte J., eds, Handbook of Exoplanets. Springer, Cham, Switzerland, p. 155

Bowler B. P. et al., 2017, AJ, 153, 18

Burruss R. S. et al., 2014, Proc. SPIE, 9148, 914827

Choquet É. et al., 2016, ApJ, 817, L2

Currie T. et al., 2013, ApJ, 776, 15

Dekany R. et al., 2013, ApJ, 776, 130

De Rosa R. J. et al., 2016, ApJ, 824, 121

Dou J., Ren D., Zhao G., Zhang X., Chen R., Zhu Y., 2015, ApJ, 802, 12

Fitzgerald M. P., Graham J. R., 2006, ApJ, 637, 541

Gerard B. L., Marois C., 2016, Proc. SPIE, 9909, 990958

Golimowski D. A. et al., 2006, AJ, 131, 3109 Hinkley S. et al., 2007, ApJ, 654, 633

Lafreniere D., Marois C., Doyon R., Nadeau D., Artigau É., 2007, ApJ, 660, 770

Lafrenière D., Marois C., Doyon R., Barman T., 2009, ApJ, 694, L148

Lagrange A. M. et al., 2009, A&A, 493, L21

Lagrange A.-M. et al., 2010, Science, 329, 57

Macintosh B. A. et al., 2008, Proc. SPIE, 7015, 701518

Macintosh B. et al., 2014, Proc. Natl. Acad. Sci., 111, 12661

Macintosh B. et al., 2015, Science, 350, 64

Marois C., Doyon R., Nadeau D., Racine R., Riopel M., Vallée P., Lafrenière D., 2005, PASP, 117, 745

Marois C., Lafreniere D., Doyon R., Macintosh B., Nadeau D., 2006, ApJ, 641, 556 Marois C., Macintosh B., Barman T., Zuckerman B., Song I., Patience J., Lafrenière D., Doyon R., 2008a, Science, 322, 1348

Marois C., Lafreniere D., Macintosh B., Doyon R., 2008b, ApJ, 673, 647

Marois C., Zuckerman B., Konopacky Q. M., Macintosh B., Barman T., 2010, Nature, 468, 1080

Marois C., Correia C., Galicher R., Ingraham P., Macintosh B., Currie T., De Rosa R., 2014, Proc. SPIE, 9148, 91480U

Masciadri E., Mundt R., Henning T., Alvarez C., Barrado y Navascués D., 2005, ApJ, 625, 1004

Mawet D., Serabyn E., Liewer K., Burruss R., Hickey J., Shemo D., 2010, ApJ, 709, 53

Mawet D., Mennesson B., Serabyn E., Stapelfeldt K., Absil O., 2011, ApJ, 738, L12

Mawet D. et al., 2014, ApJ, 792, 97

Meshkat T. et al., 2013, ApJ, 775, L40

Oh S., Price-Whelan A. M., Hogg D. W., Morton T. D., Spergel D. N., 2017, ApJ, 153, 257 (Oh17)

Oppenheimer B. R. et al., 2012, Proc. SPIE, 8447, 844720

Oppenheimer B. R. et al., 2013, ApJ, 768, 24

Pueyo L. et al., 2012, ApJS, 199, 6

Pueyo L. et al., 2015, ApJ, 803, 31

Quanz S. P., Amara A., Meyer M. R., Kenworthy M. A., Kasper M., Girard J. H., 2013, ApJ, 766, L1

Racine R., Walker G. A. H., Nadeau D., Doyon R., Marois C., 1999, PASP, 111, 587

Ren D., Dou J., Zhang X., Zhu Y., 2012, ApJ, 753, 99

Ruane G. et al., 2019, AJ, 157, 118

Ruffio J.-B. et al., 2017, ApJ, 842, 14

Schneider G., Weinberger A. J., Becklin E. E., Debes J. H., Smith B. A., 2009, AJ, 137, 53

Schneider G. et al., 2014, AJ, 148, 59

Serabyn E., Wallace K., Troy M., Mennesson B., Haguenauer P., Gappinger R., Burruss R., 2007, ApJ, 658, 1386

Serabyn E., Mawet D., Burruss R., 2010, Nature, 464, 1018

Soummer R., Aime C., 2004, in Calia D. B., Ellerbroek B. L., Ragazzoni R., eds, Proc. SPIE Vol. 5490, Advancements in Adaptive Optics. SPIE, Bellingham, p. 495

Soummer R., Ferrari A., Aime C., Jolissaint L., 2007, ApJ, 669, 642

Soummer R., Hagan J. B., Pueyo L., Thormann A., Rajan A., Marois C., 2011, ApJ, 741, 55

Soummer R., Pueyo L., Larkin J., 2012, ApJ, 755, L28

Uyama T. et al., 2017, AJ, 153, 106

Vigan A., Gry C., Salter G., Mesa D., Homeier D., Moutou C., Allard F., 2015, MNRAS, 454, 129

Wahhaj Z. et al., 2015, A&A, 581, A24

Xuan W. J. et al., 2018, AJ, 156, 156

This paper has been typeset from a TeX/LATeX file prepared by the author.